Received: 12 January 2024 | Revised: 23 April 2024 | Accepted: 19 May 2024

DOI: 10.1111/jace.19951

Journal of the American Ceramic Society

SPECIAL ISSUE ARTICLE

Correlative characterization of plasma etching resistance of various aluminum garnets

Christian Stern[1,2] | **Christian Schwab**[1] | **Moritz Kindelmann**[1,3,4] | **Mark Stamminger**[5,6] | **Thomas E. Weirich**[4] | **Inhee Park**[7] | **Florian Hausen**[7,8] | **Martin Finsterbusch**[1] | **Martin Bram**[1] | **Olivier Guillon**[1,2,9]

[1]Institute of Energy and Climate Research, Materials Synthesis and Processing (IEK-1), Forschungszentrum Jülich GmbH, Jülich, Germany

[2]Institute of Mineral Engineering, RWTH Aachen University, Aachen, Germany

[3]Ernst Ruska-Centre for Microscopy and Spectroscopy with Electrons, Materials Science and Technology (ER-C 2), Forschungszentrum Jülich GmbH, Jülich, Germany

[4]Central Facility for Electron Microscopy (GFE), RWTH Aachen University, Aachen, Germany

[5]Institute for Experimental Physics II, Ruhr University Bochum, Bochum, Germany

[6]Heraeus Noblelight GmbH, Hanau, Germany

[7]Institute of Energy and Climate Research, Fundamental Electrochemistry (IEK-9), Forschungszentrum Jülich GmbH, Jülich, Germany

[8]Institute of Physical Chemistry, RWTH Aachen University, Aachen, Germany

[9]Jülich Aachen Research Alliance, JARA-Energy, Jülich, Germany

Correspondence
Christian Stern, Institute of Energy and Climate Research, Forschungszentrum Jülich GmbH, 52425 Jülich, Germany.
Email: c.stern@fz-juelich.de

Abstract

Plasma etching is a crucial step in semiconductor manufacturing. High cleanliness and wafer-to-wafer reproducibility in the etching chamber are essential in order to successfully achieve nanometer-sized integrated functions on the wafer. The trend toward the application of more aggressive plasma compositions leads to higher demands on the plasma resistance of the materials used in the etching chamber. Due to its excellent etch resistance, yttrium aluminum garnet $Y_3Al_5O_{12}$ (YAG) is starting to replace established materials like SiO_2 or Al_2O_3 in this kind of application. In this study, reactive spark plasma sintering (SPS) was used to manufacture highly dense YAG ceramics from the respective oxides. In addition, yttrium was replaced with heavier lanthanoids (Er, Lu), intending to investigate the role of the A-site cation in the garnet type structure on the plasma erosion behavior. The produced materials were exposed to fluorine-based etching plasmas mimicking the conditions in the semiconductor manufacturing apparatus and the erosion behavior was characterized by atomic force microscopy (AFM), secondary ion mass spectrometry (SIMS), transmission electron microscopy (TEM), and profilometry. The induced chemical gradient in the samples is limited to a few nanometers below the surface, which makes its characterization challenging. For advanced analysis, we developed a correlative characterization method combining SIMS and scanning TEM (STEM)–energy-dispersive spectroscopy (EDS) enabling us to examine the structural and chemical changes in the reaction layer locally resolved. In the case of lanthanoid aluminates, an altered reaction layer and reduced fluorine penetration compared to YAG were found. However, a correlation between the characteristics of the induced chemical gradient and the determined physical erosion rates was not evident.

KEYWORDS
atomic force microscopy, etchants/etching, garnets, spark plasma sintering, transmission electron microscopy

1 | INTRODUCTION

The manufacturing of a silicon wafer is a complex process. In general, it can be divided into three different steps: patterning, etching, and doping. The most common etching technique involves applying a plasma (an ionized gas) to the wafer. This technique is a combination of physical sputtering, hence accelerated ions bombarding the wafer, and chemical etching. For more information on the fundamentals of semiconductor processing, we refer to the respective literature.[1]

Nowadays, continuous downsizing of the integrated circuits on the wafers requires more aggressive plasma compositions and leads to higher demand on cleanliness during the etching process. In order to achieve profitable production yields, process drifts, and the formation of impurity particles need to be avoided at all cost. Conventional materials for inner wall components in plasma etching applications, such as quartz glass (SiO_2) and alumina (Al_2O_3), are prone to erosion when in contact with aggressive high-density fluorine plasmas.[2,3] While the reaction products of SiO_2 are volatile, in the case of Al_2O_3 reactions with the fluorine species cause the formation of impurity particles which can be released into the semiconductor manufacturing apparatus, inducing wafer contamination.[4,5] For this reason, there is a need for the implementation of new advanced ceramics with enhanced plasma resistance. By replacing alumina with yttria, the inner wall erosion and particle generation can be significantly reduced. This can be explained by the higher formation enthalpy of yttria and the thermally more stable reaction products formed with the fluorine-based etching plasma.[6–9] Recently, yttrium aluminum garnet (YAG) has been recognized as another promising inner wall material for plasma etching chambers. First patents on semiconductor manufacturing devices with components based on YAG were reported in the late 2000s.[10,11] Kim et al.[12] and Qin et al.[5] studied the erosion behavior of YAG in fluorine-based etching plasmas in 2011 and 2012. Both used commercially available Al_2O_3 and Y_2O_3 powders as starting materials to synthesize YAG via reactive sintering of pressed compacts using vacuum furnaces. After etching in CF_4-based plasma, the erosion depth was determined using surface profilers. The results reveal excellent plasma resistance and erosion rates similar to yttria while YAG is available at a lower cost and has better mechanical properties.

With respect to the literature, the erosion of polycrystalline ceramics in fluorine-based plasmas is described as a physiochemical process including two overlapping effects. On the one hand, the surface becomes chemically degraded, which process is driven by reactive plasma species such as CF_4. On the other hand, material is physically removed by ion sputtering. Depending on the experimental parameters, the overall erosion can be more physically or chemically driven, making a clear allocation difficult.

In the past, the erosion process of ceramics in fluorine-based etching plasmas has been investigated by various characterization techniques. The surface topography is mainly studied using atomic force microscopy (AFM), profilometers or scanning electron microscopy (SEM). Secondary ion mass spectrometry (SIMS), X-ray photoelectron spectroscopy (XPS), and transmission electron microscopy (TEM) have been used to investigate the induced chemical gradients.[5,12–14]

Until today, results about plasma etching of YAG in the literature are rare and mainly focus on the physical erosion. The formation of the reaction layer is limited to the surface and does not reach deep into the bulk, which makes the characterization challenging. In a previous study on yttria, a TEM analysis reveals a thickness of the reaction layer of around 10 nm after plasma exposure for 2 h.[13] To the best of our knowledge, a comparable in-depth investigation of the reaction layer for YAG is not available until now. For this reason, the general understanding of the plasma–material interaction is still sparse.

In this study, we aim to establish a novel approach to characterize the plasma-induced chemical gradient of highly etch resistant ceramics by correlating chemical information from SIMS and structural information from scanning (S)TEM–energy-dispersive spectroscopy (EDS). For proof of our concept, YAG is used as a benchmark material and plasma parameters were chosen the same as in a previous study on yttria, where a mixed physiochemical degradation was observed.[13,14] Replacing the yttrium ion (Y^{3+}) in the garnet crystal by lanthanoids (Lu, Er) enables us to investigate the role of the A-site cations on the plasma–material interaction, aiming for enhanced plasma resistance.

Furthermore, we investigated whether characteristic values derived from the induced chemical gradient can be used to predict the plasma etch resistance under more severe etching conditions. It is hypothesized that the

substitution with heavier lanthanoid ions results in reduced plasma erosion and accordingly higher etch resistance. To minimize the influence of residual porosity on the plasma–material interaction, we applied a field-assisted sintering technology/spark plasma sintering (FAST/SPS) process to synthesize samples with a minimum amount of residual porosity in a single consolidation step.[15] FAST/SPS is a densification technique that uses direct heating of the FAST/SPS tool through a pulsed direct current (DC) and mechanical pressure at the same time. Therefore, shorter processing cycles and higher energy efficiency can be realized.[16,17]

2 | EXPERIMENTAL PROCEDURE

2.1 | Starting materials

In the present work, all aluminates have been synthesized by reactive FAST/SPS of the respective oxides. Commercial high purity Al_2O_3 (A1 grade, 99.999% purity, $d_{50} = 1.1$ µm, Heraeus Holding GmbH) and Y_2O_3 (99.999% purity, $d_{50} = 6.0$ µm, Neo Performance Materials Inc.) powders were used as raw materials to synthesize YAG ($Y_3Al_5O_{12}$). By replacing Y_2O_3 with Er_2O_3 ($d_{50} = 7.6$ µm) and Lu_2O_3 ($d_{50} = 4.6$ µm; both: 99.99% purity, Neo Performance Materials), the alternative lanthanoid aluminates erbium aluminum garnet (ErAG; $Er_3Al_5O_{12}$) and lutetium aluminum garnet (LuAG; $Lu_3Al_5O_{12}$) were created. The purity of the starting powders was confirmed using inductively coupled plasma-mass spectrometry (ICP-MS; Agilent Technologies 7900). The major impurities in the alumina powder are traces of 0.1 ppm V, 0.1 ppm Mn, 0.1 ppm Ni, and 0.8 ppm Cu. The yttria powder contains traces of 0.1 ppm Li, 0.3 ppm Na, 0.8 ppm Fe, 0.1 ppm Ba, and less than 2 ppm of lanthanoids. The major impurities in the lanthanoid oxides are Sr, Rb, Al, and other lanthanoid elements in the ppm level. The particle size distributions (PSDs) were determined with a LA950 V2 particle size analyzer (Horiba) and are summarized in the Supporting Information (Figure S1).

2.2 | Processing

The raw materials were weighed according to stoichiometry, creating batches of 250 g of each powder. The same amount of alumina grinding balls (Ø 10 mm) and 0.4 L of ethanol were added to form a slurry. After homogenization for 24 h on a roller bench, the slurry was dried using a rotary evaporator. After a subsequent sieving step (90 µm mesh), the powder was calcined for 3.5 h at 1000°C, followed by another sieving step (90 µm mesh).

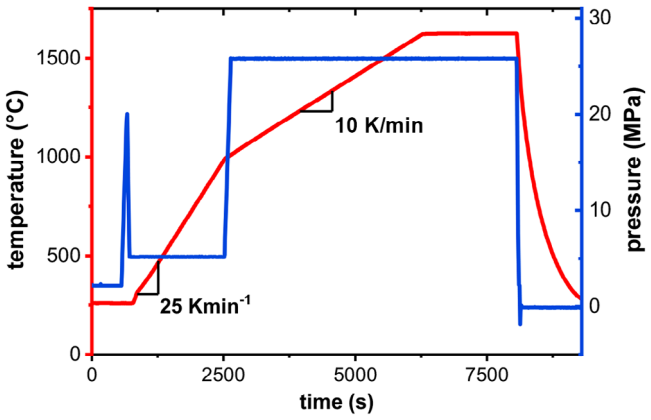

FIGURE 1 Parameters for the reactive spark plasma sintering of yttrium aluminum garnet (YAG), erbium aluminum garnet (ErAG), and lutetium aluminum garnet (LuAG).

2.3 | Reactive spark plasma sintering of Y and RE garnets

All of the aluminum garnets investigated in this study have been synthesized by reactive FAST/SPS of the respective oxides. The chemical reaction to form YAG from alumina and yttria is described as follows[18]:

$$3\ Y_2O_3 + 5\ Al_2O_3 \rightarrow 2\ Y_3Al_5O_{12}\ (YAG) \qquad (1)$$

The formation of the lanthanoid compounds follows an identical reaction, where Y is substituted by the corresponding rare earth cation (Er^{3+} or Lu^{3+}). By using reactive FAST/SPS, we can avoid sintering additives and high temperatures which are conventionally used when synthesizing YAG.[19] Here, a DSC50 (Thermal Technology LLC) FAST/SPS device was used to press 40 mm disks using a graphite die. Following a precompaction step with 20 MPa, the powders were heated at a heating rate of 25 K/min to 1000°C and then at a heating rate of 10 K/min to 1625°C while uniaxial pressure of 5 and 25 MPa was applied during the respective heating steps. Heating was followed by a 30 min dwell at 1625°C with 25 MPa pressure. Afterward, the SPS system was switched to active cooling mode. The FAST/SPS parameters are summarized in Figure 1.

2.4 | Plasma etching experiments

For plasma etching, the samples were cut in squares (10 mm × 10 mm) and the thickness was reduced below 1 mm by grinding and polishing. The last polishing step was done using colloidal silica in order to achieve a mirror-like finish and to eliminate defects that could influence

TABLE 1 Parameters for etch experiments.

Run	Samples	P_{ICP} (W)	t_{etch} (min)	p (mbar)	U_B (V)	CF_4 (sccm)	Ar (sccm)	O_2 (sccm)
1	YAG, ErAG	600	120	0.02	−150	1.0	5.0	0.3
2	LuAG	600	120	0.02	−150	0.5	5.0	0.0
3	YAG, ErAG, LuAG	600	120	0.0083	−250	1.0	5.0	0.5

Abbreviations: ErAG, erbium aluminum garnet; ICP, inductively coupled plasma; LuAG, lutetium aluminum garnet; YAG, yttrium aluminum garnet.

the erosion process. Before the plasma exposure, all samples were half masked with plasma-resistant polyimide (Kapton®) tape to induce etch steps and enable measurement of an etch rate. The sample holder and half masked samples are shown in Figure S2. A quartz glass (SiO_2) reference sample was etched in each run to keep track of process drifts and ease comparability of the different runs.

The etch experiments were conducted in an ICP plasma reactor using CF_4, Ar, and O_2 as plasma gases. Details on the experimental set up and working principle of the etch chamber can be found elsewhere.[20] The plasma parameters were chosen with respect to previous etching studies on yttria (Y_2O_3) by Kindelmann et al. that were carried out in the same etching device.[14,21] In the first etch run, YAG and ErAG were etched at the same time. In the second etch run with the LuAG sample, plasma instabilities occurred requiring an adjustment of the plasma parameters that lead to a less aggressive plasma gas composition. To investigate the influence of harsher plasma conditions, a third etch run was conducted. All samples were etched at a time to enable a sound comparison of the etch performance. Since the power of the ICP-generator (P_{ICP}) could not be further increased, it was decided to decrease the chamber pressure and increase the bias voltage. The plasma parameters are summarized in Table 1.

In yttria, Kindelmann et al. observed a shift of the dominating plasma erosion mechanisms depending on the plasma parameters.[13] In our study, we assume that the adapted plasma parameters changed these mechanisms from being more chemically driven to more physically driven.

2.5 | Characterization of starting materials and plasma–material interaction

For characterization of the microstructure after reactive SPS, the samples were ceramographically ground and polished. SEM (Ultra 55, Carl Zeiss AG) was used to analyze the microstructure.

After the plasma treatment, different characterization techniques were combined to characterize the surface and the reaction layer. AFM (Bruker Dimension Icon) was used to investigate the surface topography. Tapping mode was employed for the measurements and as cantilevers silicon tips (PPP-NCHR, NANOSENSORS, tip radius of curvature <10 nm) with Al coating on detector side and a nominal spring constant of 10–130 N/m have been used as received and calibrated individually. The results were evaluated using the software package Gwyddion (Version 2.61). Measurement artifacts like scars and strokes were removed and suitable background functions were applied to achieve comparable results.

The physical erosion of the samples etched in the third etch run was evaluated using a surface profilometer (Dektak 6M, Veeco). The step height was averaged from 4-line scans.

The induced chemical gradient that has been formed due to the plasma treatment was analyzed by means of time-of-flight (ToF) SIMS (TOF-SIMS 5 NCS, ION-TOF GmbH). A Bi^+ liquid metal ion gun was used as primary ion source operating at an energy of 30 keV and a raster size of 50 µm × 50 µm at a resolution of 128 × 128 pixels. Cs^+ ions were used as sputter ions at an energy of 1 keV in a 250 µm × 250 µm raster. Charge compensation was accomplished by a low-energy electron flood gun and Ar main flooding at a pressure of 2×10^{-6} mbar. Spectra were taken in positive and negative polarity in spectrometry mode. Crater depth was measured on the on-device attached AFM of the NCS system in contact mode. ToF-SIMS sputter times were linearly converted into a depth scale obtained from AFM measurements.

Furthermore, TEM (JEM F200, JEOL Ltd.) was used to resolve the reaction layer at the surface. High-resolution TEM (HRTEM) was used to depict the crystal structure and potential damage caused by Ar^+ sputtering during the plasma treatment. Additionally, EDS measurements using a STEM enable the characterization of the induced chemical gradients. All lamellae were extracted from a representative surface area using focused ion beam (FIB) machining (FEI Strata 400).

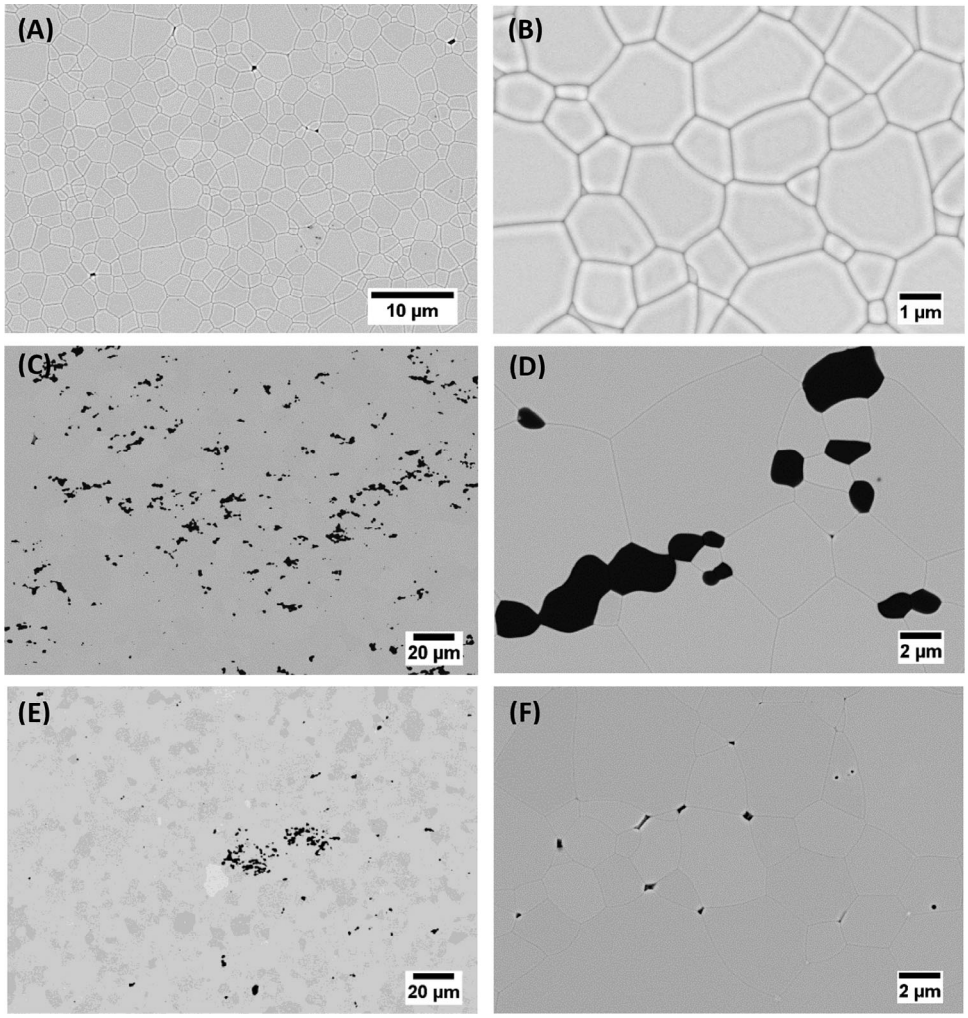

FIGURE 2 Secondary electron scanning electron microscopy (SEM) images of samples after sintering. (A, B) Yttrium aluminum garnet (YAG). (C, D) Erbium aluminum garnet (ErAG). (E, F) Lutetium aluminum garnet (LuAG).

3 | RESULTS AND DISCUSSION

3.1 | Microstructure and phase composition

Secondary electron SEM images of samples after reactive FAST/SPS sintering in the as-sintered state are shown in Figure 2. YAG (Figure 2A,B) was thermally etched at 1250°C and ErAG (Figure 2D) and LuAG (Figure 2F) at 1200°C for 30 min in order to make grain boundaries visible and get a clearer picture of the microstructure. In general, the samples are dense and homogenous, even though scattered pores are visible at triple points (Figure 2A,F). The most apparent difference between the materials is the amount of a secondary phase with dark contrast in the SEM image. This phase can clearly be identified as alumina in the SEM/EDS analysis of the etch step in the Supporting Information (Figure S3). The amount of excess alumina differs from being almost negligible in YAG, the appearance of scattered clusters in LuAG to a phase volume fraction of about 4% in ErAG. Possible reasons for this behavior are inaccuracies during the powder processing like abrasion of grinding media, differences in the alumina incorporation during homogenization or different loss on ignition (LOI) values during sintering. YAG is a line compound and therefore its phase pure synthesis is challenging.[22] The effects of nonstoichiometry on the phase evolution are complex and are considered out of scope of this study.

3.2 | Surface topography and erosion behavior

Plasma etching is a very sensitive process and small changes in the experimental parameters can have a significant impact on the results. To allow comparability of the different etch runs, one quartz glass (SiO_2) reference

TABLE 2 Overview of the conducted etch runs and erosion depth of reference samples determined by laser microscope.

Run	Samples				Erosion depth of SiO_2 reference sample (μm)
1	YAG	ErAG		SiO_2	3.3
2	LuAG			SiO_2	0.7
3	YAG	ErAG	LuAG	SiO_2	8.5

Abbreviations: ErAG, erbium aluminum garnet; LuAG, lutetium aluminum garnet; YAG, yttrium aluminum garnet.

sample was half masked and etched in every run. After etching, the erosion depth of the reference sample was determined with a laser microscope (VK-9710 Keyence Corporation). The results in Table 2 indicate that the lower CF_4 and O_2 content in the second etch run (Table 1) resulted in a significantly reduced erosion depth of the quartz glass reference sample. A possible reason for this behavior is the decreased amount of the chemically reactive species (CF_4), which leads to a smaller contribution of chemically driven erosion. Another reason could be the plasma instabilities requiring the gas composition to be adjusted in the second etch run. In the third etch run, the increase in bias voltage and decrease in chamber pressure lead to a significantly more aggressive plasma and an erosion depth of 8.5 μm on the reference sample.

To better understand the influence of the A-site ion in the garnet type structure on the etch performance, the induced etch steps in the transition zone from the etched to the shielded surface were analyzed by means of AFM. Figure 3 summarizes the results. All garnet samples did not show a well-pronounced etch step, but a contamination covering the latter. Even after multiple cleaning steps with acetone, the contamination was still present. Therefore, the respective surface area was analyzed by means of SEM/EDS. The results are summarized in the Supporting Information (Figure S3) and indicate a surface contamination with metal ions, namely, Fe and Ni. In the test reactor, the plasma interaction is not limited to the sample surface but happens in the whole chamber. The metal ions presumably originate from the chamber wall or sample holder, which are made of stainless steel.[20] The local differences in surface topography at the fringe of the polyimide tape result in a disturbed gas flow and therefore local differences in the plasma gas composition. This effect might induce the predominant redeposition of metal ions near the etch step, making a direct measurement of the erosion depth for YAG and LuAG (Figure 3A,B) very challenging. A surface treatment was not undertaken in order to preserve the as-etched status of the samples. Since the contamination is least pronounced in the ErAG sample, the topography at the etch step could still be analyzed. The black features in the etched area in ErAG (Figure 3C, white arrows) represent the former alumina secondary phase that was predominantly eroded. It is stated in the literature that alumina has a lower plasma resistance than yttria and thereby a lower plasma resistance than YAG, LuAG, and ErAG.[12] The line scans in Figure 3D show that there is almost no height difference between the etched and unetched side. This indicates that under the given conditions only minor physical erosion took place. In contrast, in previous studies on yttria, a significant amount of physical erosion was already found under comparable conditions in the same etch chamber.[13,21,23] This leads to the assumption that the materials investigated in the present study have a better plasma resistance than yttria. However, further plasma tests with harsher conditions and exchanging SiO_2 reference with Y_2O_3 reference are required to reliably benchmark these materials.

3.3 | Characterization of the reaction layer by ToF-SIMS

Even though the plasma power during the first runs was too low to trigger detectable physical erosion, the plasma still induces chemical changes at the surface of the samples. To get a better understanding of the formed reaction layer, the etched samples were examined by means of ToF-SIMS. Typically, for group 5, 6, and 7 elements as well as carbon and hydrogen, the yield of negative species in negative polarity of ToF-SIMS is higher than their respective yield as positive species in positive polarity.[24] The fluorination is the most prominent induced change in chemistry observed and fluorine is a group 7 element. Therefore, the measurements in negative polarity are preferentially used to characterize the reaction layer. However, mass interference of species can complicate the analysis. An additional measurement in different polarity can be beneficial in order to gain access to pure elements independent of other elements in species (e.g., Y^+ instead YO_2^-). The following figure shows the depth profiles of the negative species for all investigated materials as well as the depth profile of the positive species in case of YAG (Figure 4A,B). Here, the measurement in positive polarity enables access to the Y intensity independent of the oxygen profile in the YO_2^- species. Assuming constant sputter rates, the time scale of SIMS was converted to a depth scale. The results of the underlying AFM measurements are summarized in Table 3. The depth of the SIMS crater was measured directly after the SIMS measurement using the on-device attached AFM. The dimensions of the sputtering crater (250 × 250 μm) are a lot larger than the size of the holes caused by the preferentially eroded alumina phase (cf. Figure 3) and the depth of this crater was deeper than the craters caused by former alumina phase. Therefore,

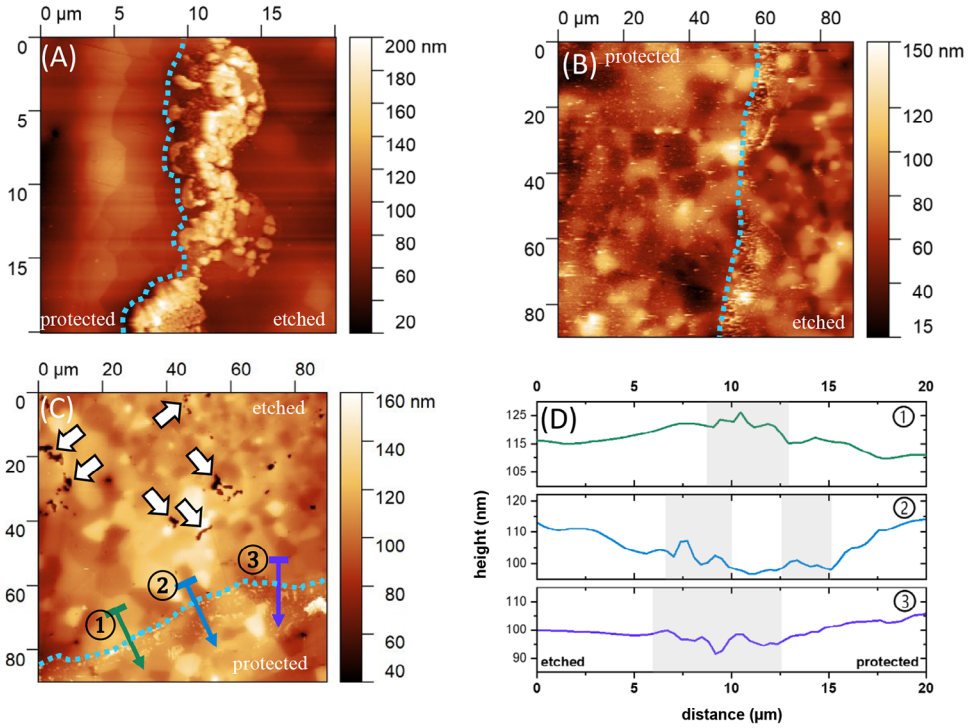

FIGURE 3 Atomic force microscopy (AFM) images of transition from etched to protected surface. (A) Yttrium aluminum garnet (YAG). (B) Lutetium aluminum garnet (LuAG). (C) Erbium aluminum garnet (ErAG). (D) Corresponding line scans to (C). Dashed blue lines indicate location of etch step. White arrows in (C) highlight former alumina phase and gray shaded areas in (D) indicate contamination.

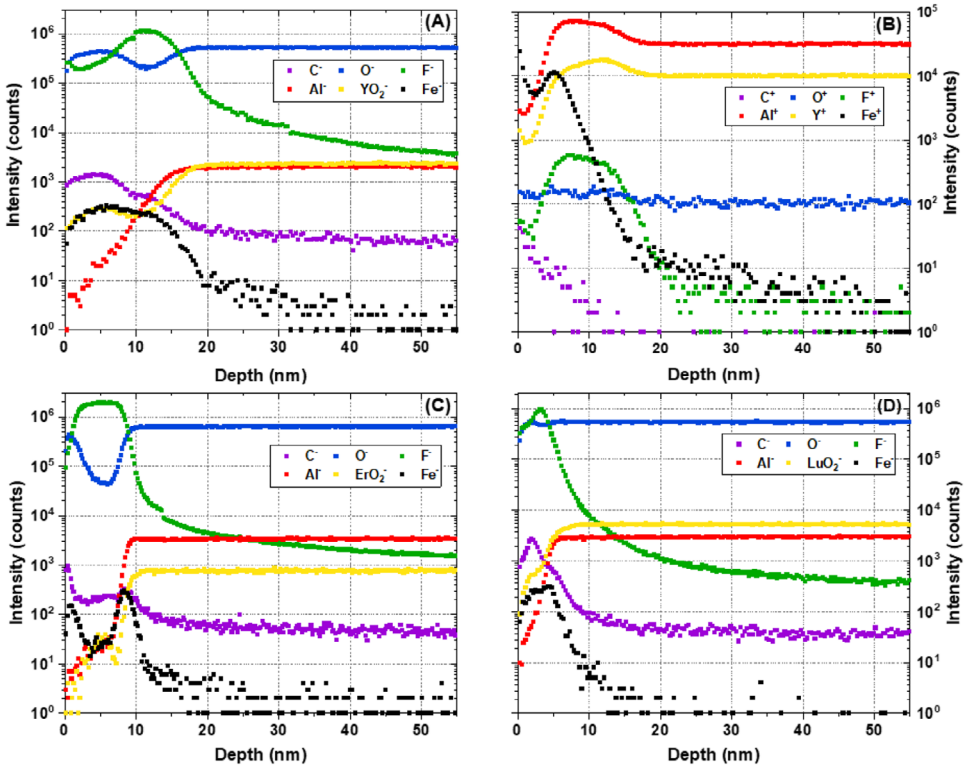

FIGURE 4 Time-of-flight secondary ion mass spectrometry (ToF-SIMS) depth profiles of all samples after plasma etching. (A) Yttrium aluminum garnet (YAG; negative polarity). (B) YAG (positive polarity). (C) Erbium aluminum garnet (ErAG; negative polarity). (D) Lutetium aluminum garnet (LuAG; negative polarity).

TABLE 3 Surface roughness R_a and depth of secondary ion mass spectrometry (SIMS) crater measured by the on-device attached atomic force microscope (AFM).

	Depth of crater (nm)	R_a (nm)
YAG	56	20
ErAG	97.5	47
LuAG	172	62

Abbreviations: ErAG, erbium aluminum garnet; LuAG, lutetium aluminum garnet; YAG, yttrium aluminum garnet.

it was possible to distinguish the different craters. The holes caused by the preferentially eroded alumina phase (Figure 3C) are a possible explanation for the differences in surface roughness (R_a). Unfortunately, high R_a values compared to the measured crater depth complicate the evaluation and are an important source of error.

In all samples, a reaction layer with altered chemical composition compared to the bulk was found. The positive and negative measurements of YAG (Figure 4A,B) illustrate the different intensities of the respective elements (except Y-species) depending on the polarity of the measurement. The fluorine and oxygen yield in the negative measurement (Figure 4A) exceed the yield in the positive measurement (Figure 4B). Vice versa the aluminum, yttrium, and iron yields in positive polarity exceed the yield negative polarity.

An assessment of critical parameters in the reaction layer has not yet been established in the literature. A possible approach is comparing the thickness of the reaction layer. However, the literature currently lacks a definition of the limits of this reaction layer. Therefore, it was decided to define the lower bound by estimating the depth at which the bulk ions reach a constant intensity. This approach results in an estimated thickness of 18 nm for YAG, 10 nm for ErAG, and 6 nm for LuAG, respectively. The reduced extent of the reaction layer hints on an enhanced chemical stability against the plasma of the erbium aluminate when comparing YAG and ErAG. In LuAG, the reaction layer is even less pronounced. But in this case, a direct comparison to YAG and ErAG is not feasible since the samples were etched in different runs with the second run being less aggressive (Table 2). Another possible value to compare the etch resistance based on the chemical gradient is the depth of fluorination. Fluorine was detected deeper in the bulk, possibly explained by Ar implantation. The depth was assessed by calculating the inflection point of the fluorine intensity using OriginPro 2020. The calculated values of 17.5 nm for YAG, 9.4 nm for ErAG, and 5.3 nm for LuAG deviate only slightly from the assessed thickness. Please note that SIMS graphs are influenced by the logarithmic intensity scale, which leads to low intensities being visually overrepresented and high intensities being compressed.

Within the reaction layer, a variation of the fluorine content is observed for all samples. This variation is characterized by a maximum of fluorine intensity close to the surface and a lower intensity zone reaching deeper into the bulk. Similar results were observed by Kindelmann et al. in a study on the etch resistance of yttria.[14] In this study, the fluorine peak is reached at a depth of 10 nm in YAG, 2 nm in ErAG, and 3 nm in LuAG. The maximum of the fluorine intensity coincides with a depletion of oxygen ions that is particularly pronounced in ErAG. A possible explanation for this is that fluorine ions occupy oxygen sites in the garnet crystal. However, subsequent TEM observations suggest that the reaction layer is mostly amorphous. Furthermore, high C^- and Fe^- concentrations were detected in the reaction layer. The presence of C^- can be attributed to the degradation of CF_4 molecules that adsorbed on the surface, whereas the Fe^- ions have been eroded from metallic components in the etch chamber. In contrast to the course of Fe^- and C^- ions, which mainly appear in the reaction layer, fluorine penetrates deeper into the bulk of the samples. This phenomenon is especially visible in YAG; whereas in ErAG and LuAG, the F^- intensity drops more significantly at the interface between reaction layer and bulk. Here, the higher atomic mass of Er and Lu when compared to Y might have an influence on the penetration depth.

To confirm that the induced chemical gradient is a consequence of interaction with the fluorine-based etching plasma an as-sintered reference sample has been ground, polished, and analyzed by ToF-SIMS. The results are given as a Supporting Information figure (Figure S4). They indicate an altered chemical composition on the sample surface up to a depth of less than 5 nm. This can be attributed to the diamond suspension and epoxy resin that was used for the sample preparation. However, deeper into the bulk, the intensities of all ions are constant. Therefore, we conclude that the ToF-SIMS measurements shown in Figure 4 represent the chemical interaction with the plasma.

Furthermore, ToF-SIMS was also employed for the characterization of the physically eroded samples. The results in the Supporting Information (Figure S5) suggest that due to the continuous erosion no reaction layer could form. The only detectable impact of the plasma is fluorination and iron implantation reaching roughly 5 nm into the sample.

3.4 | Characterization of the reaction layer by HRTEM and (S)TEM-EDS

In order to verify the thickness of the reaction layer and to support the depth-resolved SIMS measurements of the different elements, FIB lamellae have been prepared and analyzed by means of TEM and STEM-EDS. For

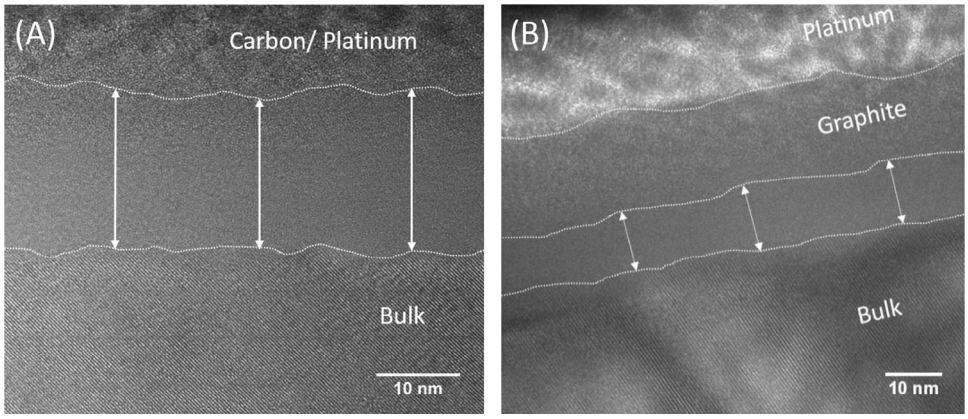

FIGURE 5 High-resolution transmission electron microscopy (HRTEM) image of (A) yttrium aluminum garnet (YAG) and (B) lutetium aluminum garnet (LuAG) after plasma exposure for 2 h. White arrows illustrate the extent of the physically damaged surface zone.

the lamella preparation using FIB machining, the samples were coated with graphite and platinum. Figure 5 shows an example of the cross section of the reaction zone in YAG and LuAG in the HRTEM mode. For ErAG, no HRTEM image could be acquired. Below the graphite and platinum coating, the TEM images of YAG and LuAG show an amorphous surface layer of roughly 20 nm in YAG and 9 nm in LuAG (marked with white arrows in Figure 5, a scattering of several nanometers is obvious). The physical damage of the garnet crystal resulting in the amorphous layer can be explained by the Ar^+ sputtering. The extent of the amorphous zone corresponds to a good extent with the thickness of the reaction layer determined by the respective SIMS measurements (18 nm for YAG and 6 nm for LuAG). Nevertheless, we can only assume whether the whole reaction layer is amorphous or whether the altered chemical composition reaches deeper into the bulk.

The induced chemical gradient was also examined by means of STEM-EDS. Figure 6 shows the integrated intensities of the relevant elements in the reaction layer after plasma exposure. The corresponding EDS mappings can be found in the Supporting Information (Figures S6–S8). The graphs can be divided into three distinct parts: (1) The graphite and platinum coating that was applied for the FIB preparation; (2) The reaction layer induced by the plasma material interaction; and (3) The bulk which is unaltered besides for the fluorination. The transition between the three parts is not clearly defined but rather merging into one another.

The high Pt and C intensities on the left side of the graphs are attributed to the conductive Pt/C coating. Because of the thickness of the C coating on the ErAG sample, the applied Pt layer was out of the measuring range, and therefore no signal is available. The increase in Fe and decrease in Pt intensity indicate the transition toward the sample surface. From the processing side, the presence of Pt in the reaction layer and Fe in the coating in YAG (Figure 7A) can be excluded. Nevertheless, they are measured in the transition zone, which might be caused by localized thickness variations of the respective layers or a nonideal (nonperpendicular) sample orientation in the analyzed area. The reaction layer is characterized by an increase of the intensities of the bulk ions (Al, O, Y/Er/Lu) and F. In YAG and LuAG, the bulk ion signals slowly increase over the whole reaction layer; whereas in ErAG, the intensities stay on a low level before they start to increase at the interface toward the unaltered bulk. The fluorination is most pronounced in ErAG and negligible in LuAG. In ErAG, the maximum of the fluorine intensity coincides with an oxygen depletion and is reached earlier compared to YAG. In all samples, the Fe intensity in the reaction layer increases, reaches a maximum after a few nanometers and decreases again when approaching the bulk of the samples. The course of the C intensity differs in the three samples. A slight but continuous decrease was observed in YAG. After a significant drop at the beginning of the reaction layer in ErAG, the intensity continues to decrease and reaches a constant level in the middle of the reaction layer. In LuAG and YAG, the course of the intensity is comparable as the intensity decreases throughout the reaction layer and attains at a constant level in the bulk. A possible explanation for the higher C intensities at the top of the reaction layer is the formation of a fluorocarbon polymer on the surface, as described by Miwa et al.[8] However, oxygen was intentionally added to inhibit the formation of such a polymer layer as it was described in the literature before.[25] Therefore, the presence of fluorocarbon polymer in the reaction layer is unlikely but cannot be excluded based on the acquired data. The interface between reaction layer and bulk can be estimated by the Fe signal approaching zero and the bulk ions (Al, Y/Er/Lu, O) reach a constant level. Again, the exact position of the interface can only be estimated. Except for the fluorination, no chemical changes could be observed

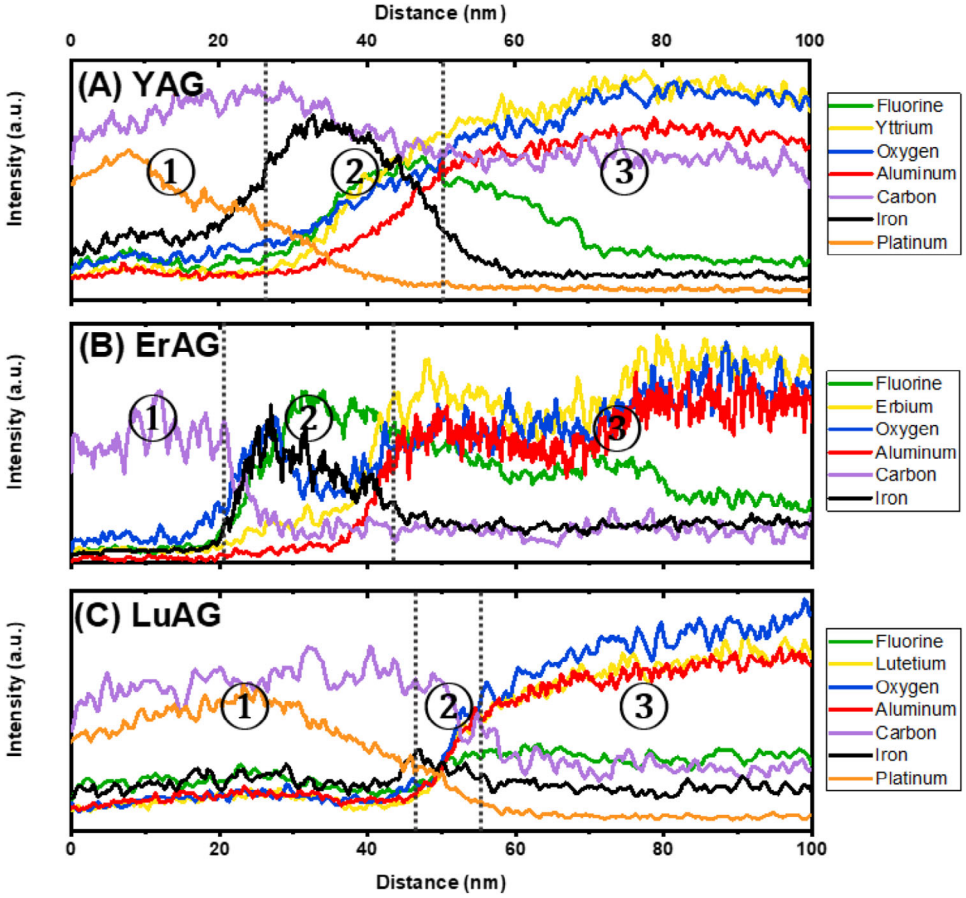

FIGURE 6 Integrated intensities acquired from scanning transmission electron microscopy (STEM)–energy-dispersive spectroscopy (EDS) of (A) yttrium aluminum garnet (YAG), (B) erbium aluminum garnet (ErAG), and (C) lutetium aluminum garnet (LuAG) after plasma exposure for 2 h. ① Platinum/graphite. ② Reaction layer. ③ Bulk.

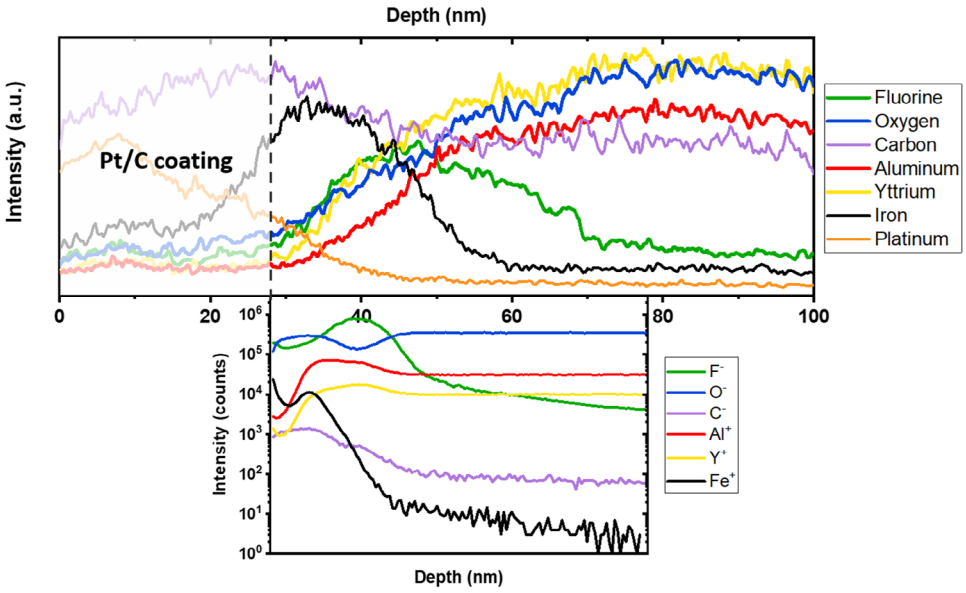

FIGURE 7 Induced chemical gradient in yttrium aluminum garnet (YAG). Correlation of scanning transmission electron microscopy (STEM)–energy-dispersive spectroscopy (EDS; top) and time-of-flight secondary ion mass spectrometry (ToF-SIMS; bottom).

in the bulk of the sample. Compared to the YAG and ErAG samples, LuAG is the least altered. A possible explanation for this behavior is the comparatively less aggressive etching environment during the second etch run (Table 2).

3.5 | Correlative characterization

ToF-SIMS and STEM-EDS enable the characterization of the induced chemical gradient, even though the information is generated in different ways. In ToF-SIMS, ions are detected by a mass spectrometer, whereas STEM-EDS uses characteristic X-rays to determine the intensities.[26,27] With the purpose of verifying the results achieved, the following section discusses the correlation of the STEM-EDS and ToF-SIMS analysis results. For the correlation of SIMS and TEM, alternative SIMS graphs showing positive or negative species of their respective measurement polarity giving a higher yield were created. F, O, and C were taken from negative polarity measurements, whereas Al, Y, Fe, and lanthanoids were taken from measurements in positive polarity. Combining measurements of two polarities also helps to avoid mass interference and enable access to uninfluenced species. In this study, the procedure enables access to the intensity of the A-site cation (Y/Er/Lu) uninfluenced by oxygen. Since SIMS does not require a conductive coating, depth profiles start at the actual sample surface. Therefore, the interface between coating and sample in STEM-EDS has been used for depth correlation by bringing this interface and the zero-position of the ToF-SIMS measurement in coincidence. Please note that the exact position of the interface can only be estimated. For the correlation, the interface was set to the same positions as in Figure 6 (dashed lines).

The correlated results of the STEM-EDS and ToF-SIMS results in YAG are shown in Figure 7. Both graphs show the same trends and especially the Fe and C intensities are in good agreement. In both measurements, the fluorine intensity rises with increasing distance from the sample surface, before it reaches a maximum toward the lower bound of the reaction layer. This maximum is reached in a lower depth in the SIMS measurement. Furthermore, the bulk ions (Al^+, Y^+, and O^-) attain a constant level in a lower depth in SIMS compared to the STEM-EDS results. A possible explanation for this is that the ToF-SIMS data are averaged over the whole analysis area (50 μm × 50 μm), whereas the STEM results are acquired on a nanometer-sized area. Furthermore, the STEM and the SIMS measurements were carried out on different parts of the sample. Another factor is the complicated depth measurement of the SIMS crater and the subsequent calculation of the sputter rate. Nevertheless, qualitative effects of plasma etching and reaction layers are well in agreement between the different methods and allow for further investigation.

The same characterization procedure was applied to ErAG. The results in Figure 8 are comparable to the results for YAG (Figure 7). Here, it has to be mentioned that the positive measurement of ToF-SIMS was stopped after reaching a sputter depth of roughly 33 nm. Therefore, the Al^+, Er^+, and Fe^+ measurements in Figure 7 do not reach deeper into the bulk. In general, both graphs show the same trends. The fluorine maximum coincides with the oxygen depletion and the increase of the bulk ions (Al, Er) only occurs toward the lower bound of the reaction layer. In this case, the difference in scaling of both graphs is even more prominent. The thickness of the reaction layer in ToF-SIMS is only about half the size of the thickness in the STEM-EDS measurement. The reasons for this are the same as mentioned for YAG: namely, different measurement spots, the data being acquired more locally in STEM, and the complicated conversion of the depth scale in ToF-SIMS.

Finally, the characterization procedure was also applied on the LuAG sample. The results are summarized in Figure 9. As for YAG and ErAG, both graphs show the same trends and the intensities are in good agreement. Compared to the YAG and ErAG samples, the induced chemical gradient is least pronounced in LuAG. Due to the low intensities, the interpretation of the fluorine and iron signal in the STEM measurement is challenging. After the correlation, the extent of the fluorination and iron penetration can be assumed with high certainty. In this case, the interpretation of the scaling of both graphs is questionable. The overlapping of the Pt and Fe intensities impedes the positioning of the interface between coating and sample and as a consequence the correlation itself.

3.6 | Physical erosion

The adjusted plasma parameters (Table 1) lead to significant erosion of all samples. The determined erosion depth and the calculated erosion rates are shown in Table 4 and compared to the characteristic values that were derived during the analysis of the induced chemical gradient. The erosion depth of YAG and ErAG in the third etch run is almost equal. However, the thickness of the reaction layer as well as the fluorination depth after etching in less aggressive plasma conditions are significantly larger in YAG compared to ErAG. This result indicates that the induced chemical gradient cannot be used to predict the resistance against plasma erosion. Furthermore, the reaction layer neither has a passivating effect nor does a less pronounced reaction layer govern enhanced plasma resistance. Since LuAG was etched in a different run, its higher

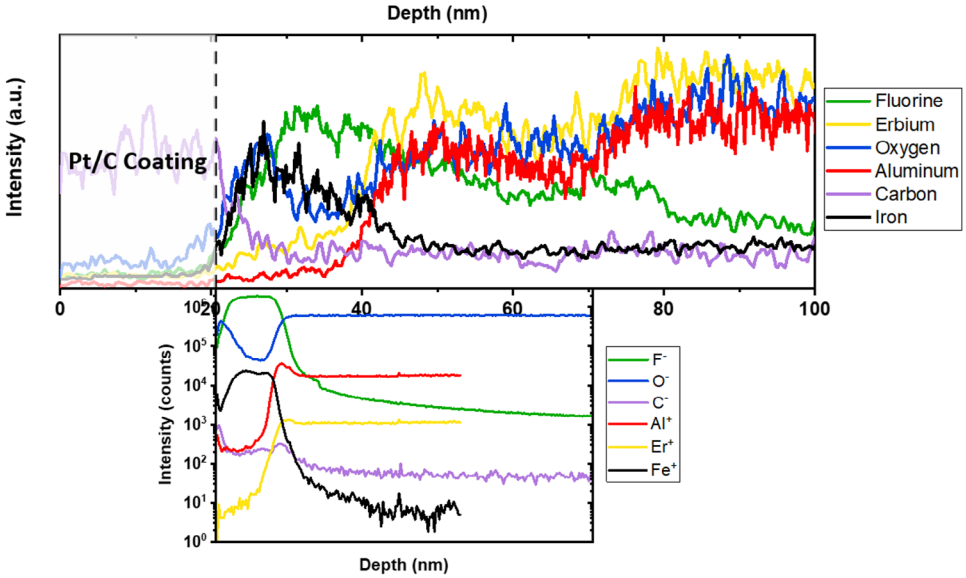

FIGURE 8 Induced chemical gradient in erbium aluminum garnet (ErAG). Correlation of scanning transmission electron microscopy (STEM)–energy-dispersive spectroscopy (EDS; top) and time-of-flight secondary ion mass spectrometry (ToF-SIMS; bottom).

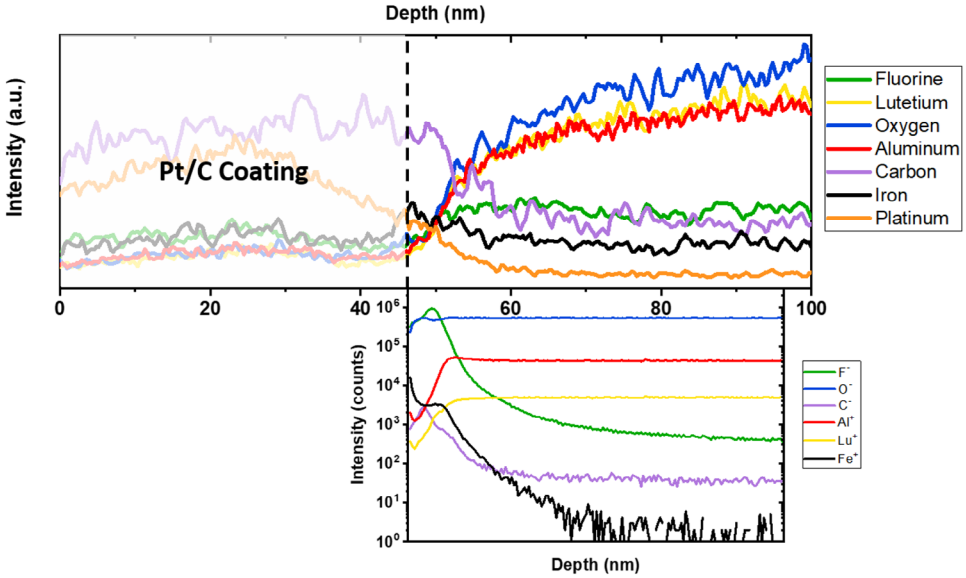

FIGURE 9 Induced chemical gradient in lutetium aluminum garnet (LuAG). Correlation of scanning transmission electron microscopy (STEM; top) and time-of-flight secondary ion mass spectrometry (ToF-SIMS; bottom).

TABLE 4 Characteristic values of the reaction layer derived from time-of-flight secondary ion mass spectrometry (ToF-SIMS; yttrium aluminum garnet [YAG], erbium aluminum garnet [ErAG]: Run 1; lutetium aluminum garnet [LuAG]: Run 2) and physical erosion determined with the surface profiler (Run 3).

Material	Thickness of reaction layer (nm)	Fluorination depth (nm)	Erosion depth (nm) in aggressive run	Erosion rate (nm/h)
YAG	18	17.5	406	203
ErAG	10	9.4	411	205.5
LuAG	6	5.3	551	275.5

erosion depth must not be linked to the values derived from the induced chemical gradient.

4 | CONCLUSIONS

In the present study, various ceramics with garnet structure (YAG, ErAG, and LuAG) have been successfully synthesized by means of reactive SPS. SEM investigations indicate a dense, homogenous microstructure, even though excess alumina has been observed in different amounts. The results of the plasma etching study indicate that all samples have a high resistance against the fluorine-based etching plasma. Two parameter sets with weaker and harsher plasma conditions were chosen. The low aggressivity of the initial plasma parameters did not trigger relevant physical erosion. Nevertheless, due to the interplay with the plasma, a mostly amorphous reaction layer was found in all samples. Additionally, a third etch run with more favorable plasma parameters was initiated that resulted in physical erosion of all samples.

Due to the absence of physical erosion in the first and second etch run established characterization methods like surface profilers or AFM fail when benchmarking these materials regarding their etch resistance and evaluating the effect when replacing Y by lanthanoid elements. For this reason, an in-depth analysis of the induced chemical gradient was carried out and characteristic values such as the thickness of the reaction layer or the fluorination depth were derived. An assessment of the plasma resistance based on this gradient has not yet been established in the literature. For a better understanding, we introduced—to our knowledge for the first time—the combination of SIMS and (S)TEM/EDS as an alternative characterization strategy. A major advantage of SIMS is that, depending on the element, the yield and thereby the intensity of the positive or negative polarity measurements are higher. This becomes especially advantageous when the intensities in STEM/EDS are comparatively low and hard to interpret. In the present study, the correlation enabled quantification of the fluorination in LuAG. Another challenge that became obvious in the present work is the appropriate scaling of the SIMS measurements. After the correlation, the scaling of the SIMS data tends to be compressed compared to the STEM results.

In the third etch run, all samples were physically eroded. The erosion depth indicates that the etch performance of YAG and ErAG is almost equal, whereas LuAG was eroded more. This is in contrast to the assessed values of the induced chemical gradient. This leads to the conclusion that the chemical gradient cannot be used to assess the plasma resistance. Furthermore, the substitution of Y^{3+} with heavier lanthanoids did not result in enhanced plasma resistance, which leads to the assumption that the A-site cation is not critical with respect to the etch resistance. Nevertheless, all materials offer excellent plasma resistance and are potential candidates for the application in semiconductor manufacturing. The results also leave room for follow-up studies using more accessible elements to substitute the yttrium ion in the garnet crystal.

For further etch experiments, the experimental setup leaves still room for improvements. As a measure to overcome the issue of etch step contamination, it is recommended to avoid metallic surfaces in the etch chamber. Metallic components that come in contact with the plasma result in the observed contamination by iron and nickel. Since the manufacturing of ceramic components with complex geometries is rather difficult, ceramic coatings such as yttria or YAG on metallic components are a promising solution.

ACKNOWLEDGMENTS

The authors acknowledge Sebastian Zischke for executing (S)TEM-EDS investigations and Doris Sebold for SEM/EDS characterizations.

Open access funding enabled and organized by Projekt DEAL.

ORCID

Christian Stern https://orcid.org/0009-0002-7254-5248
Christian Schwab https://orcid.org/0000-0002-1460-5313
Moritz Kindelmann https://orcid.org/0000-0001-9676-2090
Olivier Guillon https://orcid.org/0000-0003-4831-5725

REFERENCES

1. Mack C. Fundamental principles of optical lithography: the science of microfabrication. London: John Wiley & Sons; 2007.
2. Leech PW. Reactive ion etching of quartz and silica-based glasses in CF_4/CHF_3 plasmas. Vacuum. 1999;55(3–4):191–96. https://doi.org/10.1016/S0042-207X(99)00146-3
3. Kim D-M, Kim K-B, Yoon S-Y, Oh Y-S, Kim H-T, Lee S-M. Effects of artificial pores and purity on the erosion behaviors of polycrystalline Al_2O_3 ceramics under fluorine plasma. J Ceram Soc Jpn. 2009;117(1368):863–67. https://www.doi.org/10.2109/jcersj2.117.863
4. Tan Y, Chen P, Zhu Z, Wu S, Tian Z. Plasma etching behavior of yttrium-aluminum oxide composite ceramics. Int J Appl Ceram Technol. 2021;18(5):1710–15. https://www.doi.org/10.1111/ijac.13712
5. Qin X, Zhou G, Yang H, Wong JI, Zhang J, Luo D, et al. Fabrication and plasma resistance properties of transparent YAG ceramics. Ceram Int. 2012;38(3):2529–35. https://www.doi.org/10.1016/j.ceramint.2011.11.023
6. Miwa K, Sawai T, Aoyama M, Inoue F, Oikawa A, Imaoka K. Particle reduction using Y_2O_3 material in an etching tool. Paper presented at: 2007 international symposium on semiconductor

manufacturing; 15–17 October 2007; Santa Clara, CA, USA. https://doi.org/10.1109/ISSM.2007.4446866
7. Kim Y-C, Kim C-I. Etching mechanism of Y_2O_3 thin films in high density Cl_2/Ar plasma. J Vac Sci Technol A Vacuum Surfaces Film. 2001;19(5):2676–79. https://www.doi.org/10.1116/1.1399316
8. Miwa K, Takada N, Sasaki K. Fluorination mechanisms of Al_2O_3 and Y_2O_3 surfaces irradiated by high-density CF_4/O_2 and SF_6/O_2 plasmas. J Vac Sci Technol A Vacuum Surfaces Film. 2009;27(4):831–35. https://www.doi.org/10.1116/1.3112624
9. Kim D-M, Oh Y-S, Kim S, Kim H-T, Lim D-S, Lee S-M. The erosion behaviors of Y_2O_3 and YF_3 coatings under fluorocarbon plasma. Thin Solid Films. 2011;519(20):6698–702. https://www.doi.org/10.1016/j.tsf.2011.04.049
10. Mitsuhiro Fujita KM. Plasma-resistant member for semiconductor manufacturing apparatus and method for manufacturing the same. U.S. Patent No. 6,838,405. 2005.
11. Kobayashi Y, Ichishima M, Yokoyama Y. Plasma resistant member. U.S. Patent No. 7,090,932. 2006.
12. Kim D-M, Lee S-H, Alexander WB, Kim K-B, Oh Y-S, Lee S-M. X-ray photoelectron spectroscopy study on the interaction of yttrium-aluminum oxide with fluorine-based plasma. J Am Ceram Soc. 2011;94(10):3455–59. https://www.doi.org/10.1111/j.1551-2916.2011.04589.x
13. Kindelmann M, Weber ML, Stamminger M, Buschhaus R, Breuer U, Bram M, et al. Processing map to control the erosion of Y_2O_3 in fluorine based etching plasmas. J Am Ceram Soc. 2022;105(5):3498–509. https://www.doi.org/10.1111/jace.18334
14. Kindelmann M, Stamminger M, Schön N, Rasinski M, Eichel RA, Hausen F, et al. Erosion behavior of Y_2O_3 in fluorine-based etching plasmas: orientation dependency and reaction layer formation. J Am Ceram Soc. 2020;104(3):1465–74. https://www.doi.org/10.1111/jace.17556
15. Cao Y-C, Zhao L, Luo J, Wang K, Zhang B-P, Yokota H, et al. Plasma etching behavior of Y_2O_3 ceramics: comparative study with Al_2O_3. Appl Surf Sci. 2016;366:304–9. https://www.doi.org/10.1016/j.apsusc.2016.01.092
16. Guillon O, Gonzalez-Julian J, Dargatz B, Kessel T, Schierning G, Räthel J, et al. Field-assisted sintering technology/spark plasma sintering: mechanisms, materials, and technology developments. Adv Eng Mater. 2014;16(7):830–49. https://www.doi.org/10.1002/adem.201300409
17. Bram M, Laptev AM, Mishra TP, Nur K, Kindelmann M, Ihrig M, et al. Application of electric current-assisted sintering techniques for the processing of advanced materials. Adv Eng Mater. 2020;22(6):2000051. https://www.doi.org/10.1002/adem.202000051
18. Liu Q, Liu J, Li J, Ivanov M, Medvedev A, Zeng Y, et al. Solid-state reactive sintering of YAG transparent ceramics for optical applications. J Alloys Compd. 2014;616:81–88. https://www.doi.org/10.1016/j.jallcom.2014.06.013
19. Li J-G, Ikegami T, Lee J-H, Mori T. Low-temperature fabrication of transparent yttrium aluminum garnet (YAG) ceramics without additives. J Am Ceram Soc. 2004;83(4):961–63. https://www.doi.org/10.1111/j.1151-2916.2000.tb01305.x
20. Stamminger M. Fluorocarbon plasma erosion of silica glass doped with aluminum. Bochum: Ruhr University Bochum; 2020. https://doi.org/10.13154/294-6890
21. Kindelmann M, Weber ML, Stamminger M, Buschhaus R, Wessel E, Bram M, et al. The role of fluorination during the physicochemical erosion of yttria in fluorine-based etching plasmas. J Eur Ceram Soc. 2022;42(2):561–66. https://www.doi.org/10.1016/j.jeurceramsoc.2021.10.061
22. Cockayne B. The uses and enigmas of the Al_2O_3-Y_2O_3 phase system. J Less Common Metals. 1985;114(1):199–206. https://doi.org/10.1016/0022-5088(85)90402-3
23. Kindelmann M. Field assisted sintering of yttria ceramics for plasma etching applications. Jülich: Forschungszentrum Jülich GmbH; 2021.
24. Storms HA, Brown KF, Stein JD. Evaluation of a cesium positive ion source for secondary ion mass spectrometry. Anal Chem. 1977;49(13):2023–30. https://www.doi.org/10.1021/ac50021a034
25. Mogab CJ, Adams AC, Flamm DL. Plasma etching of Si and SiO_2—the effect of oxygen additions to CF_4 plasmas. J Appl Phys. 1978;49(7):3796–803. https://www.doi.org/10.1063/1.325382
26. Fearn S. An introduction to time-of-flight secondary ion mass spectrometry (ToF-SIMS) and its application to materials science. San Rafael, CA: Morgan & Claypool Publishers; 2015. https://www.doi.org/10.1088/978-1-6817-4088-1
27. Williams DB, Carter CB. Transmission electron microscopy. New York: Springer; 2009. https://www.doi.org/10.1007/978-0-387-76501-3

SUPPORTING INFORMATION

Additional supporting information can be found online in the Supporting Information section at the end of this article.

How to cite this article: Stern C, Schwab C, Kindelmann M, Stamminger M, Weirich TE, Park I, et al. Correlative characterization of plasma etching resistance of various aluminum garnets. J Am Ceram Soc. 2024;107:7105–18. https://doi.org/10.1111/jace.19951